



1 **Observations of creep of polar firn at different temperatures**

2

3 Yuan Li^{1,3}, Kaitlin Keegan², Ian Baker¹

4 ¹Thayer School of Engineering, Dartmouth College, Hanover, NH, 03755, USA

5 ²Department of Geological Sciences & Engineering, University of Nevada, Reno, Reno, NV,
6 89557, USA

7 ³X-Here (Future ice-based Hydrogen energy & resilient environments) Trek Laboratory
8 (Establishing), Howard Beach, NY, 11414, USA

9 *Correspondence to:* Ian Baker (ian.baker@dartmouth.edu)



10 **Abstract**

11 To improve our understanding of firn compaction and deformation processes, constant-load
12 compressive creep tests were performed on specimens from a Summit, Greenland (72°35' N,
13 38°25' W) firn core that was extracted in June, 2017. Cylindrical specimens were tested at
14 temperatures of -5°C , -18°C and -30°C from depths of 20 m, 40 m and 60 m at stresses of 0.21
15 MPa, 0.32 MPa and 0.43MPa, respectively. The microstructures were characterized before and
16 after creep using both X-ray micro-computed tomography (micro-CT) and thin sections viewed
17 between optical crossed polarizers. Examining the resulting strain vs. time and strain vs. strain
18 rate curves from the creep tests revealed the following notable features. First, the time exponent k
19 was found to be 0.34–0.69 during transient creep, which is greater than the 0.33 usually observed
20 in fully-dense ice. Second, the strain rate minimum (SRMin) in secondary creep occurred at a
21 greater strain from specimens with lower density and at higher temperature. Third, tertiary creep
22 occurred more easily for the lower-density specimens at greater effective stresses and higher
23 temperatures, where strain softening is primarily due to recrystallization. Fourth, the SRMin is a
24 function of the temperature for a given firn density. Lastly, we developed empirical equations for
25 inferring the SRMin, as it is difficult to measure during creep at low temperatures. The creep
26 behaviors of polar firn, being essentially different from full-density ice, imply that firn
27 densification is an indispensable process within the snow-to-ice transition, particularly firn
28 deformation at different temperatures connected to a changing climate.

29

30 **Keywords:** Firn; Creep; Activation energy; Microstructure; Temperature



31 **1. Introduction**

32 Understanding firm compaction and densification experimentally is critical for developing
33 physics-based firm models that are necessary for many glaciological applications, e.g. in
34 developing clean hydrogen storage technology (Li, 2023a; 2024), and on the effect related to
35 snowstorm and thunderstorm electrification (Li, et al., 2023). This motivation is thoroughly
36 described in the companion paper to this work (Li and Baker, 2022a), where the creep of firm at
37 different constant stresses at a single temperature (-10°C) was studied. The work presented, here,
38 focuses on the creep of firm at constant stress but at different temperatures. Both papers use the
39 same measurement methods and similar analysis methodologies. To avoid redundancy, we only
40 discuss the deformation of ice and firm related to the effects of temperature. It must be noted that
41 the study of the transition from firm (density $> \sim 550 \text{ kg m}^{-3}$, and porosity $< \sim 40\%$) to bubbly ice
42 ($< \sim 820\text{--}840 \text{ kg m}^{-3}$, and $> \sim 11\text{--}8\%$) is indispensable for gaining insight into how snow
43 transforms to ice. Surprisingly, the mechanical behavior of two-phase flow coupling the air flow
44 with the ice matrix deformation has not yet been performed experimentally hitherto, even though
45 the role of the microstructures of firm on air flow has been studied (Albert et al., 2000; Courville
46 et al., 2010; Adolph and Albert, 2014). This difficulty is largely due to the limitations of the
47 observation techniques of nondestructive visualization of the microstructures during snow and
48 firm deformation. Thus, caution should be taken with extending the conclusions to ice-sheet and
49 glacier-scales from sample laboratory experiments. Macroscopically, the creep of firm obeys a
50 power-law dependence of the strain rate on the stress at constant stresses and temperature, similar
51 to that of full-density ice (Li and Baker, 2022a). Note that both the diffusivity and permeability of
52 the air in the pores (Albert et al., 2000; Courville et al., 2010; Adolph and Albert, 2014) impact



53 heat conduction of the ice matrix, and hence the grain growth. This is tightly tied to the
54 micro-mechanisms, e.g. grain-boundary and lattice diffusion of the ice crystals (Li and Baker,
55 2021), superplastic deformation and inter-particle sliding from dislocation motion in the ice necks
56 (Bartelt and Von Moos, 2000), and likely rearrangement of the ice particles (Perutz and Seligman,
57 1939; Anderson and Benson, 1963; Ebinuma and Maeno, 1987). To some degree, it is not useful
58 to discuss only the deformation of snow and firn without discussing the mechanical behavior of
59 ice.

60

61 Through experiments on isotropic ice samples subjected to uni-axial compaction at octahedral
62 stresses of 0.1–0.8 MPa and temperatures from -45°C to -5°C , Jacka and Li (2000) determined
63 the mechanisms involved in the empirical *power-law flow*, which was derived by Glen (1955) for
64 stresses ranging from 0.1–1 MPa at temperatures spanning from -13°C to the melting-point. They
65 found that dynamic recrystallization predominated at higher temperatures and stresses, whereas
66 crystal rotation governed at lower temperatures and stresses. Later, Goldsby and Kohstedt (2001)
67 found that ice could exhibit *superplastic flow*, which depends inversely on the grain size,
68 particularly for fine-grained ice, while both dislocation creep and basal slip-limited creep were
69 unrelated to the grain size at stresses of 0.1 MPa or less over a wide range of temperatures.
70 Moreover, Baker and Gerberich (1979) reported that the apparent activation energy for creep for
71 polycrystalline ice, which was derived from tests at constant stress and temperatures ranging from
72 -40°C to -5°C , increased with increasing volume fraction of inclusions (bubbles, impurities, dust,
73 and the air clathrate hydrates). Such inclusions governed the evolution of grain size related to
74 thermal activations. The activation energies for the creep of snow and ice have been determined



75 by a number of authors: values ranging from 58.6–113 kJ mol⁻¹ were obtained under both uniaxial
76 and hydrostatic experiments for snow with a density of ~400 kg m⁻³ at –13.6 to –3.6°C (Landauer,
77 1958); 44.8–74.5 kJ mol⁻¹ from snow with densities of 440–830 kg m⁻³ at –34.5 to –0.5°C (Mellor
78 and Smith, 1966); ~72.9 kJ mol⁻¹ for firn with a density of 320–650 kg m⁻³ at the South Pole
79 (Gow, 1969); 69 ± 5 kJ mol⁻¹ for a mean snow density of 423 ± 8 kg m⁻³ at –19 to –11°C
80 (Scapozza and Bartelt, 2003); the 78 kJ mol⁻¹ from polycrystalline ice compression deformation
81 at a temperature of –10°C (Duval and Ashby, 1983); ~60 kJ mol⁻¹ for artificial and natural ice at
82 the South Pole (Pimienta and Duval, 1987); and 78 ± 4 kJ mol⁻¹ for monocrystal ice at –20 to –
83 4.5°C and 75 ± 2 kJ mol⁻¹ for bicrystal ice at –15 to –4.5°C (Homer and Glen, 1978). In summary,
84 the flow law of polycrystalline ice and firn depends on the effects of recrystallization, grain size,
85 inclusions (Mellor and Testa, 1969; Vickers and Greenfield, 1968; Barnes et al., 1971; Baker and
86 Gerberich, 1979; Goodman et al., 1981), and the temperature.

87

88 With advanced observation techniques, the relevant microstructural parameters of snow and firn
89 have been characterized by a number of scientists (Arnaud et al., 1998; Coleou et al., 2001; Flin et
90 al., 2004; Wang and Baker, 2013; Wiese and Schneebeli, 2017; Li, 2022). Using X-ray
91 micro-computed tomography (micro-CT), Li and Baker (2022b) characterized metamorphism
92 from snow to depth hoar under opposing temperature gradients. Only rarely has work been
93 performed on the co-effects of temperature-stress on the densification of firn while
94 simultaneously visualizing the microstructural changes using a micro-CT. For example, Schleef et
95 al. (2014) reported that densification under varying conditions of overburden stress and
96 temperature from natural and laboratory-grown new snow showed a linear relationship between



97 density and the specific surface area (SSA). To this end, the aim of our present work is to
98 investigate the temperature dependence of the creep of polar firn, and relate this to the change of
99 microstructure determined using micro-CT studies on firn obtained from Summit, Greenland in
100 2017. As is well known, temperature is a key parameter affecting the flow of firn and ice, and
101 plays a determined role in their deformation, especially for polythermal and temperate glaciers.
102 Due to the great difficulty of analyzing firn and ice deformation with the presence of liquid water,
103 this work focuses on the firn creep from the dry snow zone, i.e., areas without meltwater, at
104 different temperatures.

105

106 **2. Samples and measurements**

107 *2.1 Samples*

108 Three cylindrical samples (22 ± 0.5 mm diameter; 50 ± 0.5 mm high) were produced at each of
109 three depths of 20 m, 40 m and 60 m from the same 2017 Summit, Greenland firn core that was
110 studied in Li and Baker (2022a). Incidentally, both the densities and porosities of these above
111 samples are typical of values in the snow-to-ice transition zone as introduced in Sect. 1. More
112 importantly, samples from three depths meet the experimental requirement designed as the
113 decrease of the effective stress with increasing depth (**Appendix A**). Before creep testing, one
114 cylindrical firn samples from each depth was stored at a temperature of $-5 \pm 0.5^\circ\text{C}$, $-18 \pm 0.5^\circ\text{C}$,
115 and $-30 \pm 0.5^\circ\text{C}$ for two days to achieve thermal equilibrium (Li and Baker, 2022a).

116

117 *2.2 Creep measurements*

118 Three home-built creep jigs were placed in individual Styrofoam boxes in three different cold



119 rooms that were held at temperatures of $-5 \pm 0.5^\circ\text{C}$, $-18 \pm 0.5^\circ\text{C}$ and $-30 \pm 0.5^\circ\text{C}$. Each creep jig
120 consists of an aluminum base plate and three polished aluminum-guide rails passing through
121 linear bearings that hold the upper aluminum loading plate (Fig. 1 in Li and Baker (2022a)). A
122 linear voltage differential transducer (LVDT-Omega LD-320: resolution of 0.025%; linearity
123 error of $\pm 0.15\%$ of full scale output), parallel to the three aluminum-guide rails, was located
124 adjacent to the center of the upper plate, and fixed firmly using a screw through the plate (Fig. 1
125 in Li and Baker (2022a)) for measuring the displacement during a test. The displacement was
126 logged every 5 seconds using a Grant SQ2010 datalogger (accuracy of 0.1%). Temperatures were
127 logged at 300-second time intervals over the entire test period, using a k-type thermocouple
128 (Omega RDXL4SD thermistor: resolution of 0.1°C) that was mounted inside each box. In this
129 work, specimens were tested at temperatures of $-5 \pm 0.2^\circ\text{C}$, $-18 \pm 0.2^\circ\text{C}$ and $-30 \pm 0.2^\circ\text{C}$ -the
130 smaller error bars for the temperature of the specimens than the room temperature deviation is
131 because the creep jigs were in insulated Styrofoam boxes-from depths of 20 m (applied stress
132 0.21 MPa), 40 m (0.32 MPa) and 60 m (0.43 MPa). These stresses were chosen based on
133 experience from previous tests (Li and Baker, 2022a) in order to give measurable creep rates in a
134 reasonable time.

135

136 *2.3 X-ray micro computed tomography (micro-CT)*

137 Each specimen at each depth and temperature combination was scanned using a Skyscan 1172
138 micro-CT, before and after creep testing. Each micro-CT scan lasted ~ 2 hours. The cubic Volume
139 of Interest (VOI, a side length of 8 mm) was taken from near the center of the firm specimen as
140 conducted in Li and Baker (2022a). The microstructural parameters obtained from the micro-CT



141 data are the SSA, the mean structure thickness of the ice matrix (S.Th), the area-equivalent circle
142 diameter of the pores (ECDa), the total porosity (TP), the closed porosity (CP), and the structure
143 model index (SMI). The SSA (mm^{-1}) is the ratio of the ice surface area to total firm volume (ice
144 plus air) in a VOI analytical element, and is calculated using the hexahedral marching cubes
145 algorithm via CTAn software (Wang and Baker, 2013). It characterizes the thickness and
146 complexity of the firm microstructure. Changes in SSA indicate a change in free energy of the ice
147 surfaces, the decrease of which represents the occurrence of sintering-pressure. The S.Th (mm) is
148 the mean structure thickness of an ice matrix (Hildebrand and Ruesgsegger, 1997), which
149 represents the characteristic size of an ice particle in the firm, where the ice particle consists of one
150 or many crystals or grains. It is measured based on the largest sphere diameter that encloses a
151 point in the ice matrix and is completely bounded within solid surfaces. The ECDa (mm) is the
152 diameter of a circle having the same area as the measured on average from 2-D binary images for
153 all pores involved in a computed VOI, indicative of the characteristic size for the void space
154 (Adolph and Albert, 2014). The TP (%) is the ratio of the pore volume, including both open and
155 closed pores, to the total VOI. The CP (%) is the ratio of the volume of the closed pores to the
156 total volume of solid plus closed pores volume in a VOI, while the open porosity (%) is the ratio
157 of the volume of the open pores to the total VOI. The SMI is calculated based on the dilation of a
158 3-D voxel model (Hildebrand and Ruesgsegger, 1997) as $SMI = 6(S' \times V) / S^2$, where S' is the
159 change in the surface area due to dilation, and V and S are the object volume and surface area,
160 respectively. It indicates the prevalent ice curvature, negative values of which represent a concave
161 surface, e.g. the hollow air structure surrounded by an ice matrix. The more negative the SMI
162 value, the more spherical the pore. Notably, the micro-CT-derived density of each specimen



163 agrees well with the bulk density measured using the mass-volume approach (Li and Baker,
164 2021).

165

166 *2.4 Thin section preparation and imaging*

167 Thin sections for optical photographs before and after creep testing were cut from bulk specimens,
168 one side of which was first smoothed with a microtome. This side was then frozen onto a glass
169 plate (100 × 60 × 2 mm) by dropping supercooled gas-free water along its edges. Its thickness
170 was reduced to ~2 mm by a band saw, and finally thinned further to a uniform thickness of ~0.5
171 mm using a microtome. Images were captured using a digital camera after each thin section was
172 placed on a light table between a pair of crossed polarizing sheets.

173

174 **3 Results and discussion**

175 *3.1 Microstructures before creep*

176 Increasing firm density with increasing depth from either of the -5°C , -18°C , and -30°C
177 specimens can be readily recognized by visual inspection of the micro-CT 3-D reconstructions of
178 the firm microstructure (**Figure 1**). Correspondingly, the microstructural parameters, with the
179 exception of the CP, changed monotonically with increasing depth at each temperature, e.g. the –
180 30°C samples increased in density from $591 \pm 1.4 \text{ kg m}^{-3}$, to $683 \pm 4.2 \text{ kg m}^{-3}$, to $782 \pm 1.5 \text{ kg m}^{-3}$,
181 decreased in SSA from $4.64 \pm 0.04 \text{ mm}^{-1}$, to $3.3 \pm 0.06 \text{ mm}^{-1}$, to $2.39 \pm 0.01 \text{ mm}^{-1}$, and decreased



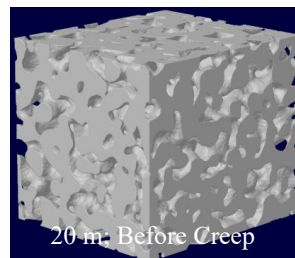
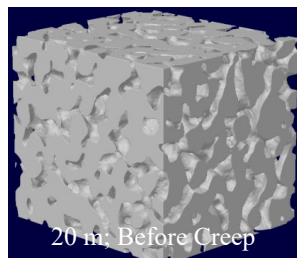
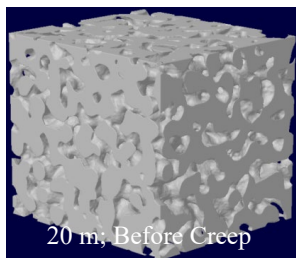
182

-5°C

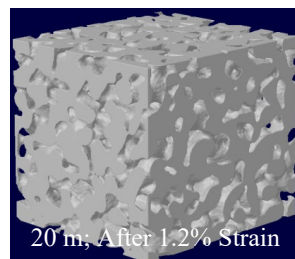
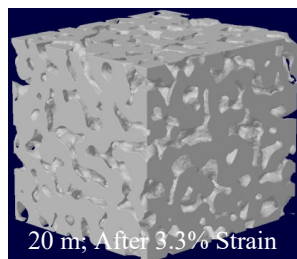
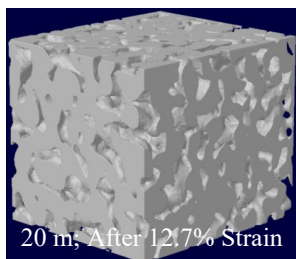
-18°C

-30°C

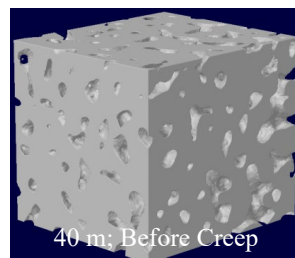
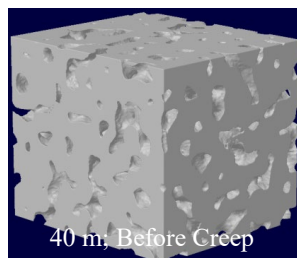
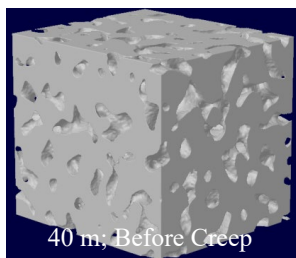
183



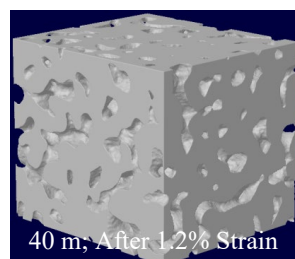
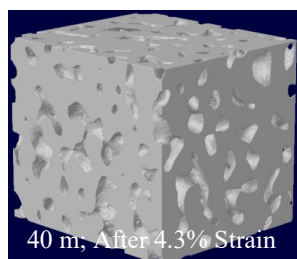
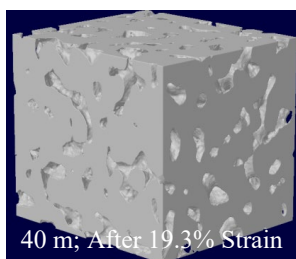
184



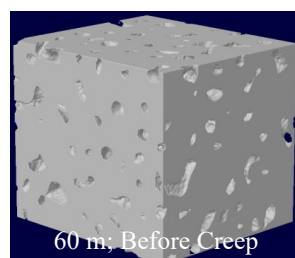
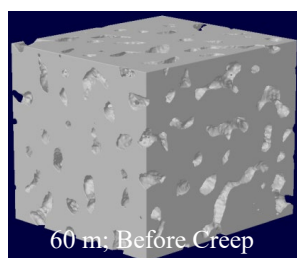
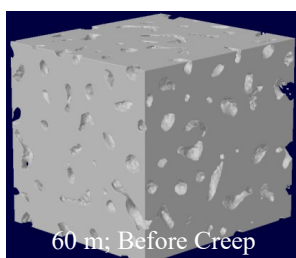
185

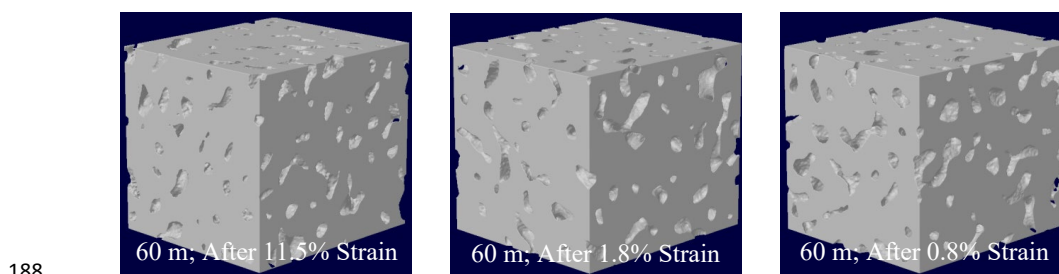


186



187





188
 189 **Figure 1:** Micro-CT 3-D reconstructions (the side length of each cubic volume of interest is 8 mm)
 190 of specimens before and after creep testing at the depths and temperatures shown. Grey voxels
 191 represent ice in the firm structure.

192

193

194 Table 1. Microstructural parameters derived from Micro-CT for samples at -5°C , -18°C , and $-$
 195 30°C from depths of 20 m, 40 m, and 60 m before creep.

| 20m | | | | | | | |
|-------------------------|-------------------------------|-------------------------|--------------|-----------|-------------|------------|--------------|
| T $^{\circ}\text{C}$ | Density kg m^{-3} | SSA mm^{-1} | S.Th mm | TP % | CP % | SMI | ECDa mm |
| -5 | 589±1.3 | 4.74±0.03 | 0.732±0.001 | 35.9±0.08 | 0.03±0.002 | -0.31±0.04 | 1.07±0.005 |
| -18 | 615±2.5 | 4.51±0.04 | 0.758±0.001 | 33.1±0.2 | 0.01±0.001 | -0.57±0.01 | 0.995±0.013 |
| -30 | 591±1.4 | 4.64±0.04 | 0.747±0.004 | 35.6±0.05 | 0.02±0.001 | -0.27±0.05 | 1.09±0.004 |
| 40m | | | | | | | |
| T $^{\circ}\text{C}$ | Density kg m^{-3} | SSA mm^{-1} | S.Th mm | TP % | CP % | SMI | ECDa mm |
| -5 | 685±1.4 | 3.26±0.04 | 0.95±0.004 | 25.5±0.1 | 0.015±0.001 | -1.85±0.11 | 0.857 ±0.005 |
| -18 | 669±0.6 | 3.41±0.04 | 0.914±0.003 | 27.1±0.03 | 0.01±0.001 | -1.69±0.09 | 0.892±0.002 |
| -30 | 683±4.2 | 3.30±0.06 | 0.94±0.01 | 25.6±0.4 | 0.021±0.005 | -1.87±0.13 | 0.86±0.01 |
| 60m | | | | | | | |
| T $^{\circ}\text{C}$ | Density kg m^{-3} | SSA mm^{-1} | S.Th mm | TP % | CP % | SMI | ECDa mm |
| -5 | 790±1.0 | 2.34±0.03 | 1.1±0.003 | 14.0±0.1 | 0.11±0.01 | -4.81±0.22 | 0.594±0.003 |
| -18 | 780±0.5 | 2.37±0.03 | 1.08±0.01 | 15.2±0.06 | 0.014±0.007 | -4.8±0.2 | 0.632±0.001 |
| -30 | 782±1.5 | 2.39±0.01 | 1.076±0.0003 | 14.8±0.2 | 0.02±0.001 | -4.92±0.14 | 0.639±0.002 |

198



199 in TP from $35.6 \pm 0.05\%$, $25.6 \pm 0.4\%$, to $14.8 \pm 0.2\%$ at 20, 40, and 60 m, respectively (**Table 1**).
200 These above changes are similar to those previously observed in this firn core (Li and Baker,
201 2022a), implying that the sintering-pressure mechanism plays a crucial role in the densification of
202 polar firn due to the increasing overburden of snow and firn with increasing depth. However, the
203 microstructures of the samples from the three temperatures at each depth shows little variability
204 and does not monotonically change with temperature, e.g. at 20 m depth the -5°C , -18°C , and $-$
205 30°C samples having densities of $589 \pm 1.3 \text{ kg m}^{-3}$, $615 \pm 2.5 \text{ kg m}^{-3}$, and $591 \pm 1.4 \text{ kg m}^{-3}$, and
206 SSAs of $4.74 \pm 0.03 \text{ mm}^{-1}$, $4.51 \pm 0.04 \text{ mm}^{-1}$, and $4.64 \pm 0.04 \text{ mm}^{-1}$, respectively (**Figures 1–2**;
207 **Table 1**). Here, the -18°C specimen being denser than the two others at -5°C and -30°C is not
208 able to be concluded that the sintering of firn is not directly related to the temperature. This is
209 likely because the duration of two days during thermal equilibration in the absence of
210 compression is too short to sufficiently exert the influence of temperature on firn sintering. The
211 microstructural differences seen in these specimens more likely arose from the initial samples
212 themselves, which were anisotropic and heterogeneous even if taken from the same depth,
213 attributed to firn pre-deformation and partial anneal before experiments (Li and Baker, 2022a).

214

215 3.2 Microstructures after creep

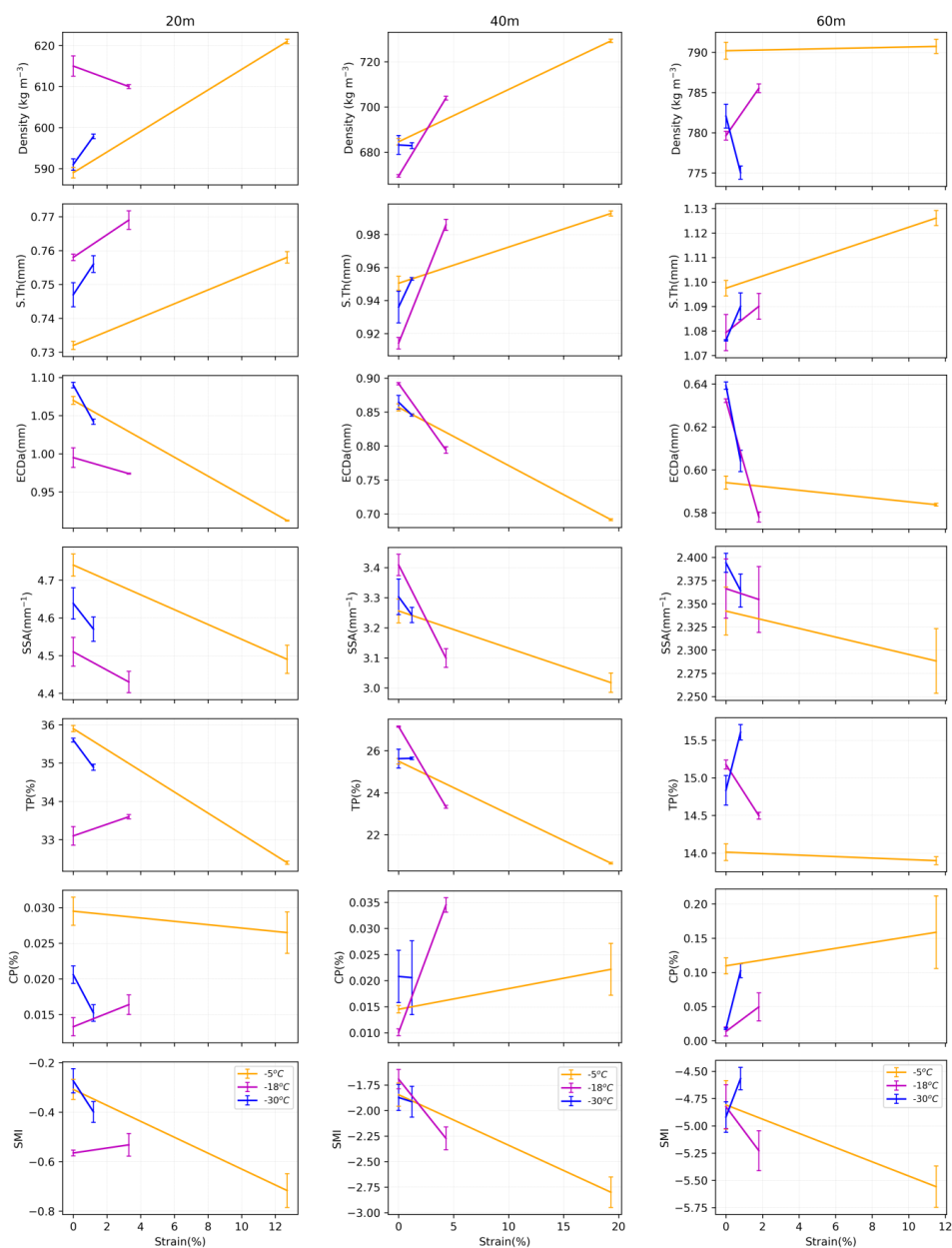
216 The microstructural evolution can be characterized well by the microstructural parameters in
217 **Figure 2**. The largest changes occur in the -5°C specimens due to the higher temperature, i.e., the
218 density, S.Th, and CP increased, while the ECDa, TP, SSA and SMI decreased, indicative of
219 consolidation of the firn after creep. It is important to note that for the 60 m sample tested at -5°C
220 there was no change in density, i.e. $790.2 \pm 1 \text{ kg m}^{-3}$ before creep vs. $790.7 \pm 0.9 \text{ kg m}^{-3}$ after



221 creep, or TP, i.e. $14.0 \pm 0.1\%$ before creep vs. $13.9 \pm 0.1\%$ after creep. These lack of
222 microstructural change is due to the high initial density, which was close to the firm pore close-off
223 density of $\sim 830 \text{ kg m}^{-3}$. Thus, the creep of this sample may involve a transition from firm to
224 bubbly ice, as also indicated with the increase in CP, which would have made it difficult to
225 compress further. Intriguingly, some of the changes in microstructure observed in the micro-CT
226 3-D reconstructions from the specimens before and after creep, e.g. the distribution of ice-space,
227 are indistinguishable in **Figure 1**. This is presumably due to the relatively large initial particle size,
228 or from radial dilation exceeding the axial compression because of the small strains that occurred
229 at the relatively low temperatures.

230

231 One exception to the expected microstructural change after creep was the decrease of CP, which
232 was likely due to the measurement uncertainty of the micro-CT (Burr et al., 2018), or the radial
233 dilation of the specimen during creep. Another exception was the decrease in density after creep
234 for the -18°C specimen at 20 m and the -30°C specimen at 60 m, which was due to temperature
235 gradient metamorphism, as confirmed by the increase of both TP and S.Th (Li and Baker, 2022b).
236 The rate of firm densification should decrease with increasing depth at a given temperature, due to
237 the decrease of effective stress with increasing depth (**Appendix A**). As a matter of fact, the
238 density of the -5°C samples after creep increased by 32 kg m^{-3} , 44 kg m^{-3} , and 0.5 kg m^{-3} for the
239 20 m, 40 m, and 60 m samples, respectively. The 44 kg m^{-3} unexpectedly outnumbers the 32 kg
240 m^{-3} , implying that the densification of firm is also affected by other undetermined factors, e.g. the
241 effect of inclusions, in addition to the stress and temperature.



242

243 **Figure 2:** Density, structure thickness (S.Th), area-equivalent circle diameter (ECDA), specific
 244 surface area (SSA), total porosity (TP), closed porosity (CP), and structure model index (SMI) of
 245 the firm samples before and after creep at three temperatures (orange, magenta, and blue lines)



246 from depths of 20 m, 40 m and 60 m. Error bars indicate the variation of each microstructural
247 parameter as derived from three different VOIs of the same sample.

248

249

250 Another way to investigate microstructure changes before and after creep tests is to compare their
251 grain sizes using thin sections. As an example, **Figure 3** shows optical micrographs of thin
252 sections made from the -5°C sample at 40 m before and after creep to a strain of 19.3%, where
253 the significant reduction in grain size from 0.8 ± 0.17 mm to 0.53 ± 0.18 mm implies the
254 occurrence of recrystallization during testing. However, it is also unclear at what strain
255 recrystallization

256

257

258

259

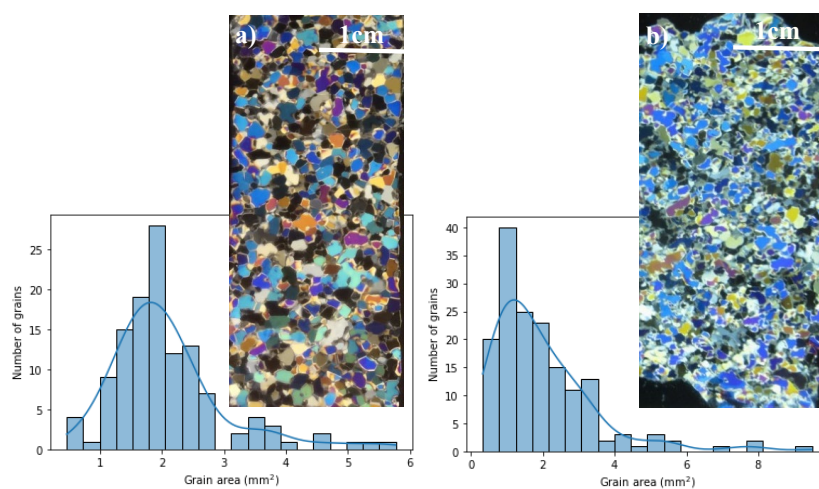
260

261

262

263

264



265 **Figure 3:** Optical micrographs of thin sections, and the distribution of grain sizes for the 40 m sample
266 at -5°C (a) before and (b) after creep (19.3% strain).

267

268



269 was initiated in each test, as noted in Li and Baker (2022a). Recrystallization occurs frequently at
270 a temperature higher than the homologous temperatures of $0.9 T_m$, however no evidence was
271 found for recrystallization after testing at the relatively cold -18°C and -30°C conditions,
272 probably due to the small creep strains at these relatively low temperatures. The creep
273 mechanisms for these samples, and whether the mechanisms were different at different
274 temperatures, could not be determined from the micro-CT-derived microstructural observations
275 alone. This is because the micro-CT can only capture the microstructure before and after creep.
276 Instead, plots of both strain vs. time and strain rate vs. strain can be used to elucidate the onset of
277 recrystallization during creep (Sects. 3.3 and 3.4; Ogunmolayusi, et al., 2023).

278

279 *3.3 Relationship between strain and time*

280 **Figure 4** shows the strain vs. time creep curves. The specimens at -5°C at 20 m, and at -18°C at
281 20 m, 40 m and 60 m, show decelerating transient creep and quasi-viscous steady-state creep,
282 while the specimens at -5°C at 40 m and 60 m show transient, secondary, and accelerating tertiary
283 creep. Note that the curves from the -30°C specimens are not easily interpreted, due to a large
284 amount of noise arising from both the insufficient resolution of a linear voltage differential
285 transducer (Li and Baker, 2022a) and the very small strains. The transient creep stage may be
286 caused by strain hardening that occurs from the yield point to the ultimate strength. The plastic
287 deformation is accommodated by an increase in dislocation density through dislocation
288 multiplication or the formation of new dislocations, which leads to an increase of the firm strength
289 as the dislocations become pinned or tangled, and thus more difficult to move. The initial
290 decrease of creep rate may also be related to the rearrangement of dislocations into a more stable



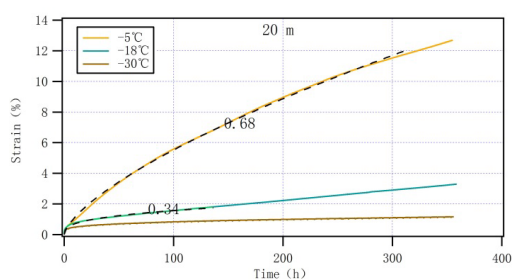
291 pattern through a dragging mechanism (Weertman, 1983) for the -5°C specimens. The tertiary
292 creep stage may be associated with strain softening deriving either from the thermally-activated
293 processes at the high homologous temperature approaching the melting point of ice, or from
294 recrystallization (Li and Baker, 2022a). Clearly, the creep rate of firm is sensitive to temperature
295 under a constant stress at a given depth, *viz.*, the creep rate increases with increasing temperature
296 (**Figure 4**). Incidentally, there is no evidence of the onset of recrystallization in the creep curves
297 themselves despite the thin-section observation that -5°C specimens clearly underwent
298 recrystallization during creep (Sects. 3.2).

299

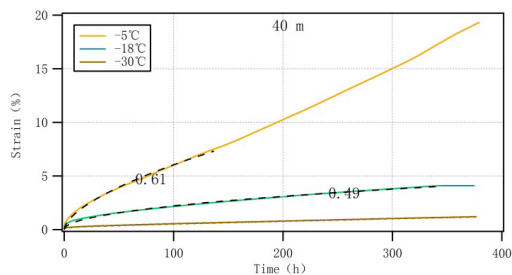
300 A modified Andrade-like equation $\varepsilon = \beta t^k + \varepsilon_0$ in Li and Baker (2022a) was used to describe the
301 transient creep behavior of the firm, in which the primary creep was well represented in black
302 dashed lines on the creep curves in **Figure 4**. The time exponent k , derived from the above
303 equation, ranges from 0.34–0.69: the data for the -30°C specimens are excluded since the noise in
304 the results makes them uninterpretable. These k values are also smaller than those from
305 monocrystalline and bicrystalline ice: 1.9 ± 0.5 , 1.5 ± 0.2 , and 1.3 ± 0.4 (Li and Baker, 2022a and
306 references therein). We also note that the k values from the specimens at -5°C from 20–60 m
307 (0.68, 0.61, and 0.69), and at -18°C from 40 m (0.49) are greater than 0.33, while the k value
308 from the -18°C specimens at 20 m (0.34) and 60 m (0.34) are close to 0.33 that is usually
309 obtained for full-density polycrystal ice. These k values imply that the more the constraints from
310 the grain-boundaries, the slower the deformation rate will be, and that the grains in firm deform
311 with less grain-boundary constraints than in a full-density polycrystalline ice because of the
312 presence of void space in firm (Li and Baker, 2022a; Li, 2023b). Clearly, the above k values,



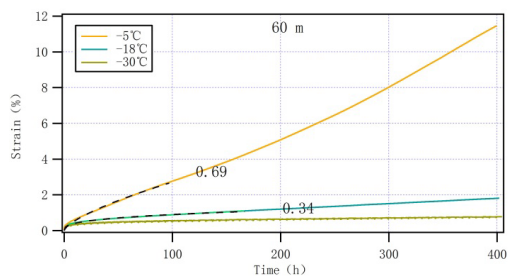
313



314



315



316

317 **Figure 4:** Strain vs. time for firm specimens at -5°C (red lines), -18°C (green lines), and -30°C
318 (blue lines), from depths of 20 m (applied stress 0.21 MPa), 40 m (0.32MPa) and 60 m (0.43MPa).

319 The black dashed curves represent fits to a modified Andrade-like equation with the time
320 exponents indicated on the curves, if any.

321

322

323 which increased with increasing temperature (**Figure 4**), indicate that deformation is easier

324 because of the lower viscosity at the higher temperature. Thus, k seems to be a state variable with



325 respect to temperature. In addition, k values greater than 0.33 may be related to the decrease of
326 viscosity of the firm specimens (Freitag et al., 2002; Fujita et al., 2014). These features seem to be
327 simpler than those in Li and Baker (2022a), where some k values were lower than 0.33, likely
328 suggesting that the effect of temperature overwhelmed the effect of impurities during creep of
329 polar firm. Alternatively, the enhanced cohesion strength in the firm, which resulted from both the
330 ice matrix with higher purity and the stronger bond connection of inter-grains, increases the
331 viscosity of test samples and lowers the k value to less than 0.33.

332

333 *3.4 Relationship of strain rate to strain*

334 **Figure 5** shows log strain rate vs. strain plots from all the -5°C and -18°C specimens; the -30°C
335 samples are excluded due to noise. The evolution of the strain rate is characterized more clearly in
336 **Figure 5** than in **Figure 4**. Clearly, the strain rate is also a state variable of temperature, where the
337 strain rate increases with increasing temperature for a given strain at a given depth (**Figure 5**;
338 **Table 2**). The strain rate minimum at the secondary creep stage (SRMin) and the strain at the
339 SRMin for all the -5°C and -18°C specimens are shown in **Figure 5** and **Table 2**. The SRMin was
340 reached at a strain of 11.8%, 7.5% and 2.7% for the -5°C specimens from depths of 20 m, 40 m,
341 and 60 m, respectively, consistent with strains at the SRMin decreasing with increasing depth at a
342 given temperature in **Figure 7** and **Table 3** in Li and Baker (2022a). For the -18°C specimens, the
343 SRMin occurred over a range of strains from 1.81–2.9% at 20 m, at a fixed strain of 4.1% at 40 m,
344 and at a strain oscillating between 1.1 and 1.8% at 60 m. These values of strain at different
345 SRMin values are different from those usually observed at strains of 0.5–3% for fully-dense ice
346 (e.g. Cuffey and Paterson, 2010), implying that different mechanical behavior between firm and



347 Table 2. Observed and inferred strain rate minima and strains observed at the strain rate minima.

| 20 m | SRMin s ⁻¹ | PC1-SRMin s ⁻¹ | PC2-SRMin s ⁻¹ | PC3-SRMin s ⁻¹ | Strain % |
|----------|--------------------------|------------------------------|------------------------------|------------------------------|-------------|
| -5°C | 5.53×10 ⁻⁶ | 5.53×10 ⁻⁶ | 1.68×10 ⁻⁶ | 2.56×10 ⁻⁷ | 11.8 |
| -18°C | 1.36×10 ⁻⁶ | 1.36×10 ⁻⁶ | 2.29×10 ⁻⁷ | 2.45×10 ⁻⁸ | 1.81–2.9 |
| -30°C(U) | – | 7.14×10 ⁻⁷ | 2.17×10 ⁻⁷ | 3.3×10 ⁻⁸ | – |
| -30°C(L) | – | 3.16×10 ⁻⁸ | 9.6×10 ⁻⁹ | 1.46×10 ⁻⁹ | – |

348

| 40 m | SRMin s ⁻¹ | PC1-SRMin s ⁻¹ | PC2-SRMin s ⁻¹ | PC3-SRMin s ⁻¹ | Strain % |
|----------|--------------------------|------------------------------|------------------------------|------------------------------|-------------|
| -5°C | 1.03×10 ⁻⁵ | 3.39×10 ⁻⁵ | 1.03×10 ⁻⁵ | 1.57×10 ⁻⁶ | 7.5 |
| -18°C | 1.4×10 ⁻⁶ | 8.32×10 ⁻⁶ | 1.40×10 ⁻⁶ | 1.5×10 ⁻⁷ | 4.1 |
| -30°C(U) | – | 4.37×10 ⁻⁶ | 1.33×10 ⁻⁶ | 2.03×10 ⁻⁷ | – |
| -30°C(L) | – | 1.94×10 ⁻⁷ | 5.88×10 ⁻⁸ | 8.97×10 ⁻⁹ | – |

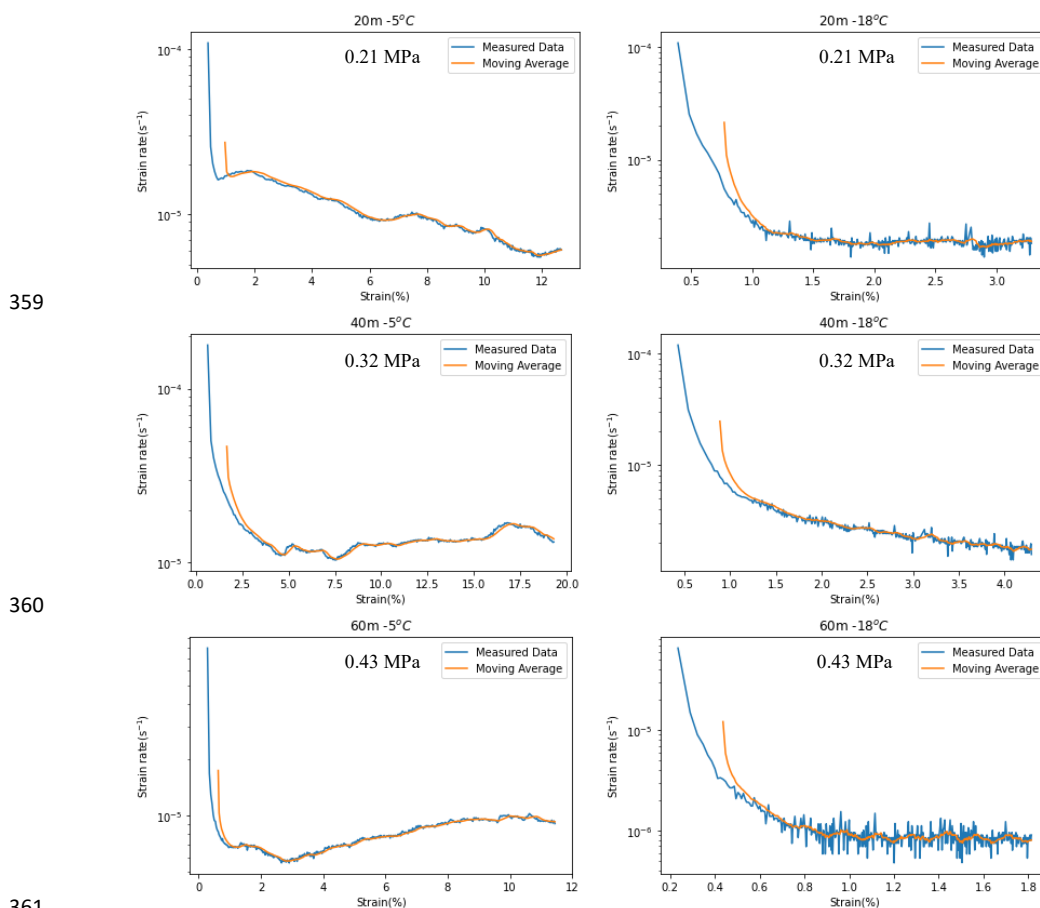
349

| 60 m | SRMin s ⁻¹ | PC1-SRMin s ⁻¹ | PC2-SRMin s ⁻¹ | PC3-SRMin s ⁻¹ | Strain % |
|----------|--------------------------|------------------------------|------------------------------|------------------------------|-------------|
| -5°C | 5.59×10 ⁻⁶ | 1.21×10 ⁻⁴ | 3.67×10 ⁻⁵ | 5.59×10 ⁻⁶ | 2.7 |
| -18°C | 5.33×10 ⁻⁷ | 2.96×10 ⁻⁵ | 4.99×10 ⁻⁶ | 5.33×10 ⁻⁷ | 1.1–1.8 |
| -30°C(U) | – | 1.56×10 ⁻⁵ | 4.74×10 ⁻⁶ | 7.21×10 ⁻⁷ | – |
| -30°C(L) | – | 6.91×10 ⁻⁷ | 2.1×10 ⁻⁷ | 3.19×10 ⁻⁸ | – |

350 The SRMin without the prefix is the observed values during creep, while the SRMin with a prefix
 351 is the inferred values. Note that PC-SRMin is the abbreviation of the post-calibration SRMin, and
 352 that -30°C(U) and -30°C(L) indicate the upper and lower bound from the -30°C samples from
 353 44.8 kJ mol⁻¹ and 113 kJ mol⁻¹, respectively. PC1-SRMin, PC2-SRMin, and PC3-SRMin are
 354 described in **Appendix B**. The symbol – indicates the unavailable values of SRMin and the strain
 355 value at the SRMin observed during creep. The color fonts and backgrounds are described in
 356 **Appendix B**.

357

358



362 **Figure 5:** Log strain rate vs. strain from the firm specimens at temperatures of -5°C and -18°C
363 from depths of 20 m (applied stress 0.21 MPa), 40 m (0.32MPa) and 60 m (0.43MPa). Samples
364 from -30°C are not shown due to the very large noise. The blue lines represent discrete strain rates,
365 which are calculated by extracting the strain data hourly, while the orange lines represent a
366 moving average of 15 moving windows with respect to the strain.

367

368

369 pure ice (Li and Baker, 2022a). Overall, the strain at the SRMin is greater with lower density and
370 higher temperature, e.g. 11.8% strain from the -5°C specimens at 20 m, 4.1% strain from the –



371 18°C specimens at 40 m, where a larger strain was caused by the longer-lasting strain hardening
372 (Li, 2023b). Additionally, tertiary creep occurs both during quasi-steady state deformation (from
373 the –5°C specimens at 40 m and 60 m) and in the ascending stage (from the –5°C and –18°C
374 specimens at 20 m and the –18°C specimen at 40 m) more easily with lower firn density, greater
375 effective stress, and higher creep temperature, e.g. from the –5°C specimens at 20 m, where the
376 strain softening is primarily due to recrystallization.

377

378 3.5 Apparent activation energy for creep

379 Experimental observations of the SRMin are sparse and limited, as they only occurred for the –
380 5°C and at –18°C specimens at each depth (**Table 2**). It is hard to achieve the SRMin for all firn
381 specimens in laboratory environments (Landauer, 1958), especially under low temperatures and
382 stresses such as those from the –30°C specimens in this work. To this end, we offer the various
383 possibilities of the SRMin using the evidence we have.

384

385 First, we attempted to estimate the apparent activation energy of creep, Q_c (kJ mol⁻¹), by
386 rearranging the Arrhenius relation $\dot{\epsilon}=A\sigma^n \exp(-Q_c/RT)$ to $Q_c = -R[\partial \ln(\dot{\epsilon}/\sigma^n)/\partial(1/T)]$,
387 where $\dot{\epsilon}$ (s⁻¹) is the strain rate, A (s⁻¹ Pa⁻ⁿ) is the creep exponent factor, σ (MPa) is the applied
388 stress, n is the creep (stress) exponent, R (8.314 J mol⁻¹ K⁻¹) is the gas constant, and T (K) is
389 Kelvin temperature, on the basis of *only* two SRMins from the –5°C and –18°C samples at each
390 depth (**Table 2**). The Q_c values from the 20 m, 40 m, and 60 m specimens were calculated to be
391 61.4 kJ mol⁻¹, 87.3 kJ mol⁻¹, and 102.8 kJ mol⁻¹, respectively (**Figure 6**). Based on the three
392 SRMins from the –5°C and –18°C samples at 60 m in this work, and from –10°C samples at 60 m



393 in Li and Baker (2022a), a Q_c value for the 60 m specimen was calculated to be $100.7 \text{ kJ mol}^{-1}$.
394 To see whether or not these above Q_c values are reliable, we estimated the activation energy of
395 grain-boundary diffusion/viscosity, Q_{gbd} (kJ mol^{-1}), using the relation
396 $K = (D_t^2 - D_0^2)/t = k \exp(-Q_{\text{gbd}}/RT)$, in an alternative form of $Q_{\text{gbd}} = -R[\partial \ln K / \partial (1/T)]$,
397 where K is the observed rate of grain growth ($\text{mm}^2 \text{ a}^{-1}$), D_0^2 and D_t^2 are the measured mean
398 grain area (mm^2) in a firm sample at the onset of the creep ($t = 0$), and at the end time of the creep
399 (t -year), and k is a constant grain growth factor. The grain growth rates are plotted on a
400 logarithmic scale against the reciprocal of T (**Figure 6**). For changes in grain size from the related
401 specimens before and after creep see Li and Fu (2024). Correspondingly, the Q_{gbd} values
402 calculated were 41.4 kJ mol^{-1} , 40.8 kJ mol^{-1} , and 40.9 kJ mol^{-1} for the specimens at 20 m, 40 m,
403 and 60 m, respectively. These Q_{gbd} values are comparable to the values of 40.6 kJ mol^{-1} obtained
404 in laboratory experiments on polycrystalline ice (Jumawan, 1972), and 42.4 kJ mol^{-1} from 13
405 polar firn cores (Cuffey and Paterson, 2010) for grain-boundary self-diffusion of polycrystalline
406 ice. Further, the ratio of Q_{gbd}/Q_c is 0.67, 0.47, and 0.4 for the 20 m, 40 m, and 60 m specimens,
407 respectively. We noted that the ratio of 0.67 for Q_{gbd}/Q_c was recommended by Hobbs (1974) and
408 Cuffey and Paterson (2010). The Q_c values calculated using the Arrhenius relation for the 40 m
409 and 60 m specimens are likely greater than the actual values, and hence are seemingly less
410 reliable. There is little difference between the two-SRMin-derived Q_c value ($102.8 \text{ kJ mol}^{-1}$) and
411 the three-SRMin-derived Q_c value ($100.7 \text{ kJ mol}^{-1}$), implying that these two methods for
412 calculating Q_c have equal utility. Moreover, the above Q_{gbd} values are lower than the 48.6 kJ
413 mol^{-1} that was inferred by the grain growth rate for firn samples with densities ranging from 320–
414 650 kg m^{-3} from cores drilled at South Pole, Antarctic (Gow, 1969), which makes a ratio of 0.67



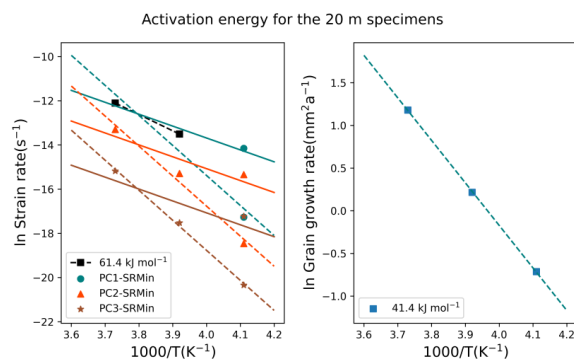
415 for Q_{gbd}/Q_c an unreliable sole-criterion. In short, it is difficult to assess the reliability of both Q_c
416 and Q_{gbd} , as discussed above due to their scatter and debates in the current literature. Thus, these
417 Q_c values estimated in this work ranging from 61.4–102.8 kJ mol⁻¹ are reasonable, falling within
418 the range of 44.8–113 kJ mol⁻¹ reported in the literature (**Table 3**).

419

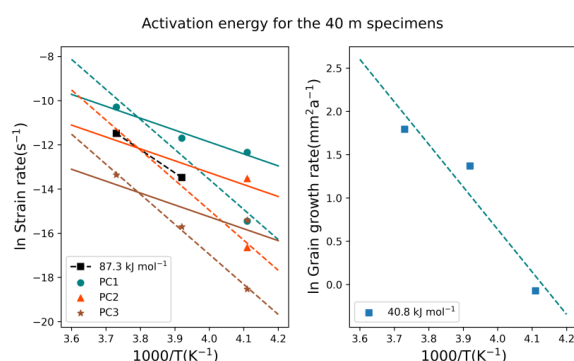
420 A great challenge is the estimation of the Q_c using the SRMins including the –30°C specimens,
421 whose SRMin shows high variability due to the extraordinarily slow strain rate at low
422 temperatures. This difficulty cannot be resolved by extrapolating experimental data (Sinha, 1978;
423 Hooke et al., 1980), e.g. the use of Andrade’s law (Glen, 1955). Instead, we turned our focus to
424 studying the relationship between the SRMin and temperature by constraining our data in a wide
425 range of Q_c values reported in the literature presented in Table 3. Clearly, there is a larger scatter
426 of Q_c values for firm than for ice. The increase of Q_c from mono-crystalline and bi-crystalline
427 to polycrystalline ice implies that the fewer the constraint of grain-boundaries, the greater is Q_c .
428 Alternatively, firm creep is easier than that of polycrystalline ice due to either the easier sliding of
429 grains in firm along more directions in the more porous and heterogeneous structure (Sect. 3.3), or
430 the decrease of viscosity associated with inclusions (e.g. Baker and Gerberich, 1979; Goodman et
431 al., 1981) that facilitate the intra- and inter-grain sliding (Salamatin et al., 2009).



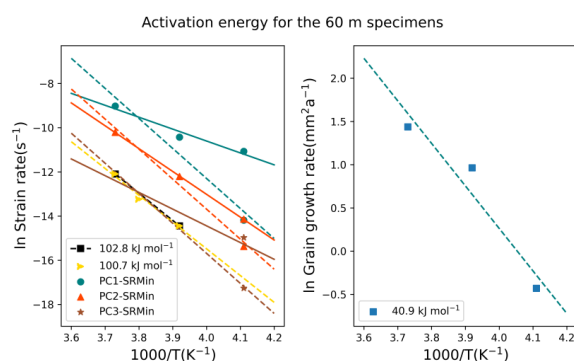
432



433



434



435

436 **Figure 6:** Arrhenius plots to estimate the apparent activation energy of creep (Q_c ; left panel) and
 437 the apparent activation energy of grain-boundary diffusion (Q_{gbd} ; right panel) from the firm
 438 specimens noted. The blue, magenta, and red solid lines are the upper bound (44.8 kJ mol⁻¹) of
 439 PC1-SRMin, PC2-SRMin, and PC3-SRMin, respectively, while the blue, magenta, and red dashed
 440 lines are the lower bound (113 kJ mol⁻¹) of PC1-SRMin, PC2-SRMin, and PC3-SRMin,



441 respectively (Table 2). The blue circles, the magenta triangles, and the red stars are the data in
 442 Table 2. The black dashed lines are from *only* two SRMins at -5°C and -18°C (the black squares
 443 are the data measured), whose Q_c is indicated in each subfigure. The green dashed line is from the
 444 three SRMins at -5°C , -18°C in this work, and -10°C from Li and Baker (2022a) (the green
 445 triangles are the measured data), whose Q_c is $110.7 \text{ kJ mol}^{-1}$. The blue dashed lines (right panel)
 446 are from grain growth rate at three temperatures (the blue squares are the observed data), whose
 447 Q_{gbd} is indicated in each subfigure.

448

449

450 Table 3. Apparent activation energy for the creep of firn and ice, Q_c , reported in literature.

| Q_c kJ mol^{-1} | Sample | Density kg m^{-3} | Temperature $^{\circ}\text{C}$ | Methods | Source |
|-------------------------------|--|-------------------------------|-----------------------------------|--|------------------------------|
| 58.6–113 | Firn | ~400 | $[-13.6, -3.6]$ | Uniaxial/Hydrostatic Compression | Landauer (1958) |
| 44.8–74.5 | Firn/Bubbly Ice | 440–830 | $[-34.5, -0.5]$ | Uniaxial Unconfined Compression | Mellor & Smith (1966) |
| 54 | Firn/Bubbly Ice | Undetail ed | $[-28, -16]$ | Shear Deformation of Boreholes | Paterson (1977) |
| ~72.9 | Firn | 320–650 | Unnecessary | Grain Growth Rate | Gow (1969) |
| 69 ± 5 | Firn | 423 ± 8 | $[-19, -11]$ | Triaxial Compression | Scapozza & Bartelt (2003) |
| ~60 | Artificial/Natural Ice (South Pole) | ~917 | -15 | Torsion Creep Test | Pimienta & Duval (1987) |
| 61 | Polycrystalline Ice | ~917 | -9.6 | Hydrostatic Pressure | Duval et al. (1983) |
| 78 | Monocrystalline Ice | ~917 | $[-30, -4]$ | Derived from Bicrystal Ice | Homer & Glen (1978) |
| 75 | Ice Bicrystal | ~917 | $[-30, -4]$ | Tensile Test Parallel to Grain-boundary | Homer & Glen (1978) |

451

452



453 In principle, Q_c of firm should exceed that for polycrystalline ice. Intriguingly, some reported
454 Q_c values from firm are less than that for ice, meaning the degree of spatial freedom in the
455 ice-matrix is limited by the topological structure of the firm (Liu et al., 2022). Incidentally, the
456 effective stress of porous materials is determined by not only its porosity, but also other factors,
457 e.g. the microstructural topology (Liu et al., 2022) and the impurity types and concentrations in
458 the firm. However, this issue is beyond the scope of this work. In summary, a Q_c for firm, which
459 ranges from 44.8–113 kJ mol⁻¹, is plausible due to the intrinsic nature of natural firm that has a far
460 more complicated and changeable microstructure than ice.

461

462 The stress exponent n is calculated from the measured SRMins (**Table 2**) to be ~ 0.1 and ~ -1.2
463 from the -5°C and -18°C samples, respectively, using Glen's law $\dot{\epsilon} = A\sigma^n$. This is in
464 disagreement with the reported $n = \sim 4.3$ by Li and Baker (2022a). Thus, the SRMin value from all
465 the samples must be calibrated via a constraint from the n values. To proceed, the post-calibration
466 SRMins for the -5°C and -18°C samples are highlighted in Table 2 (see **Appendix B** in detail).
467 From here on we only discuss the applied stress since there is little difference between the
468 effective stress and applied stress for calculating the stress exponent (Li and Baker, 2022a). Based
469 on both the reported range of Q_c and the two observed SRMins at -5°C and -18°C , the SRMins
470 for the -30°C samples are inferred (**Table 2**), using the Arrhenius relation.

471

472 Also, based on both the observed and inferred SRMins with the upper and lower bounds (**Table 2**),
473 a series of fitted functions are then found between the SRMin and the reciprocal of the
474 temperature ($^\circ\text{C}$), $1/T_c$:



475

$$\left\{ \begin{array}{l} \text{SRMin} = -3 \times 10^{-5} / T_c - 7 \times 10^{-7} [R^2 = 0.988; \text{PC 1(L 20)}] \\ \text{SRMin} = -3 \times 10^{-5} / T_c - 2 \times 10^{-7} [R^2 = 1; \text{PC 1(U 20)}] \\ \text{SRMin} = -1 \times 10^{-5} / T_c - 3 \times 10^{-7} [R^2 = 1; \text{PC 2(L 20)}] \\ \text{SRMin} = -9 \times 10^{-6} / T_c - 2 \times 10^{-7} [R^2 = 0.987; \text{PC 2(U 20)}] \\ \text{SRMin} = -2 \times 10^{-6} / T_c - 6 \times 10^{-8} [R^2 = 0.998; \text{PC 3(L 20)}] \\ \text{SRMin} = -1 \times 10^{-6} / T_c - 3 \times 10^{-8} [R^2 = 0.976; \text{PC 3(U 20)}] \end{array} \right\}$$

477

$$\left\{ \begin{array}{l} \text{SRMin} = -2 \times 10^{-4} / T_c - 4 \times 10^{-6} [R^2 = 0.988; \text{PC 1(L 40)}] \\ \text{SRMin} = -2 \times 10^{-4} / T_c - 2 \times 10^{-6} [R^2 = 1; \text{PC 1(U 40)}] \\ \text{SRMin} = -6 \times 10^{-5} / T_c - 2 \times 10^{-6} [R^2 = 1; \text{PC 2(L 40)}] \\ \text{SRMin} = -6 \times 10^{-5} / T_c - 1 \times 10^{-6} [R^2 = 0.987; \text{PC 2(U 40)}] \\ \text{SRMin} = -1 \times 10^{-5} / T_c - 3 \times 10^{-7} [R^2 = 0.998; \text{PC 3(L 40)}] \\ \text{SRMin} = -9 \times 10^{-6} / T_c - 2 \times 10^{-7} [R^2 = 0.976; \text{PC 3(U 40)}] \end{array} \right\}$$

479

$$\left\{ \begin{array}{l} \text{SRMin} = -7 \times 10^{-4} / T_c - 2 \times 10^{-5} [R^2 = 0.988; \text{PC 1(L 60)}] \\ \text{SRMin} = -6 \times 10^{-4} / T_c - 6 \times 10^{-6} [R^2 = 1; \text{PC 1(U 60)}] \\ \text{SRMin} = -2 \times 10^{-4} / T_c - 7 \times 10^{-6} [R^2 = 1; \text{PC 2(L 60)}] \\ \text{SRMin} = -2 \times 10^{-4} / T_c - 4 \times 10^{-6} [R^2 = 0.987; \text{PC 2(U 60)}] \\ \text{SRMin} = -3 \times 10^{-5} / T_c - 1 \times 10^{-6} [R^2 = 0.998; \text{PC 3(L 60)}] \\ \text{SRMin} = -3 \times 10^{-5} / T_c - 7 \times 10^{-7} [R^2 = 0.976; \text{PC 3(U 60)}] \end{array} \right\}$$

481

482 where PC1(L20) and PC1(U20) indicate the lower and upper bound values of the post-calibration
 483 SRMins from the 20 m samples (**Table 1**), and other symbols are similarly formatted, e.g.
 484 PC1(L40), PC1(U40), PC1(L60), PC1(U60), and so on. These relationships are plotted in **Figure**
 485 **7**, where the SRMin vs. $1/T_c$ plots from the three depths are almost the same shape, implying that
 486 the SRMin is dependent on the temperature at a constant stress. It is important to note that the
 487 average (minimum) strain rate for the secondary creep stage for a given temperature increases



488

489

490

491

492

493

494

495

496

497

498

499

500

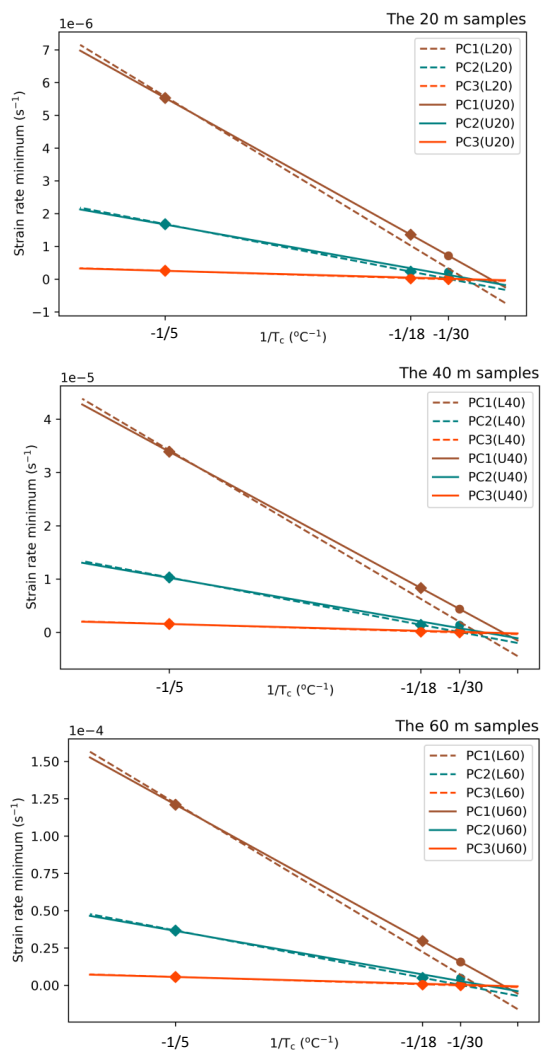
501

502

503

504 **Figure 7:** Plots of the strain rate minimum versus the reciprocal of temperature. PC1(L20) and
505 PC1(U20) indicates the lower and upper bound, respectively, from the 20 m samples via PC1 as
506 noted in Table 2, and so on. The circles indicate the upper bound data measured and inferred,
507 while the squares indicate the lower bound data. The dashed line is the fit from the lower bound,
508 while the solid line is the fit from the upper bound.

509





510 with increasing depth/density of the samples (**Figure 7; Table 2**). This is opposite to a decrease of
511 the SRMin at a fixed stress and temperature in **Figure 7** and **Table 3** in Li and Baker (2022a).
512 These changes in SRMin are irrespective of the stress (**Appendix A**). The temperature plays a
513 predominant role during firm creep for a given density of sample at a constant stress. An
514 interesting question on firm creep at a specific temperature is whether the SRMin slows down or
515 speeds up with decreasing density of firm. Certainly, natural firm samples raise the complexity in
516 interpreting the firm creep due to the influences both from inclusions (Li and Baker, 2022a and
517 references therein; Li, 2024), and from the topology of the microstructures (Liu et al., 2022). In
518 addition, there is a broad spread of the SRMin at each depth, in which the SRMin varies by
519 several times, even one order of magnitude or more between the different possibilities of
520 post-calibration SRMins (**Figure 7**), implying that the microstructure of the sample significantly
521 influences the process of the creep of firm. Moreover, it is hard to generalize a universal formula
522 for predicting the SRMin at temperatures below -30°C , where the SRMins becomes negative
523 (**Figure 7**). Thus, there is a need for an in-depth understanding of the polar firm creep behavior in
524 secondary creep stage.

525

526 To illustrate the differences between the Q_c values calculated from PC1-SRMin, PC2-SRMin,
527 and PC3-SRMin, we have plotted them in **Figure 6**. Interestingly, the Arrhenius plots of the
528 natural logarithm of strain rate with $1000/T$ (**Figure 6**) are similar to those observed by Glen
529 (1955) and Homer and Glen (1978), implying that there is no significant difference in the creep
530 mechanism for a temperature range of -30°C to -5°C (Glen, 1955; Homer and Glen, 1978), where
531 both diffusion via grain-boundary, vacancy or interstitial defects (Barnes et al., 1971; Brown and



532 George, 1996; Nasello et al., 2005; Li and Baker, 2022b) and dislocations contribute to the creep
533 of polar firn.

534

535 **4. Conclusions**

536 Constant-load creep tests were performed on three cylindrical specimens tested from depths of 20
537 m (applied stress 0.21 MPa), 40 m (0.32MPa) and 60 m (0.43MPa) at temperatures of $-5 \pm 0.2^\circ\text{C}$,
538 $-18 \pm 0.2^\circ\text{C}$, and $-30 \pm 0.2^\circ\text{C}$ from a firn core extracted at Summit, Greenland in June, 2017. The
539 microstructures were characterized before and after creep testing using the micro-CT and thin
540 sections viewed between optical crossed polarizers. It was found that:

541

542 1. Microstructural parameters measured using the micro-CT show that the polar firn densified
543 during the creep compression (e.g. from 685 to 729 kg m^{-3} for the 40 m specimen at -5°C),
544 *viz.*, the TP (from 25.5 to 20.7%), the ECDA (from 0.86 to 0.69 mm), the SSA (from 3.26 to
545 3.02 mm^{-1}), and the SMI (from -1.85 to -2.8) decreased, while the S.Th (from 0.95 to 0.99
546 mm) and the CP (from 0.01 to 0.02%) increased. Anomalies in the microstructures, especially
547 at low temperatures of -18°C and -30°C , are likely due to metamorphism under temperature
548 gradients, the radial dilation effect during firn deformation, the measurement uncertainty of
549 the micro-CT, or the anisotropy and the heterogeneity of natural firn.

550 2. The transient creep behavior of firn at constant stress and different temperatures obeys an
551 Andrade-like law, but, the time exponent k of 0.34–0.69 is greater than the 0.33 found for ice.
552 This is due to fewer grain-boundary constraints in porous firn than in ice.

553 3. The secondary creep behavior of firn at constant stress and different temperatures presented



554 here shows that the strain at the SRMin increases with decreasing firm density and increasing
555 creep temperature. In particular, low-density firm during creep at high temperatures shows that
556 the strain at the SRMin, e.g. 11.8% and 7.5% respectively from the 20 m and 40 m specimens
557 at -5°C , is greater than the strain of 3% that is the maximum found at the SRMin of ice.

558 4. The tertiary creep behavior of firm at constant stress and different temperatures is more easily
559 observed from lower-density specimens at greater effective stresses and higher creep
560 temperatures. The strain softening in tertiary creep is primarily due to recrystallization.

561 5. The apparent activation energy for the firm creep has a wide range of $61.4\text{--}102.8\text{ kJ mol}^{-1}$
562 because the grains in firm slide more easily along more directions in the more porous and
563 heterogeneous structure, the enhanced fluidity from inclusions, and the topological structure
564 of the firm. In addition, the SRMin is a function of the temperature, depending on the
565 microstructure of firm and the inclusion content. The predicted SRMin increases with
566 increasing firm density at a given temperature, and is independent on the effective stress.
567 Lastly, there is no significant difference in creep mechanism at temperatures ranging from $-$
568 30°C to -5°C .

569

570 The creep of polar firm behaves differently from full-density ice, implying that firm densification is
571 an indispensable process in fully understanding the transformation of ice from snowfall in the
572 polar areas. Observed firm deformation indicates that temperature plays a determined role in firm
573 densification. Thereby, it will be helpful to bridge a gap between the firm temperature and climate
574 of the past for reconstructing paleoclimate. Also, it will be helpful to apply a confining load to
575 investigate the microstructure of the creep of polar firm with smaller initial particle sizes at low



576 temperatures using the micro-CT. Further studies of interest are to investigate the quantitative
577 relationship between the microstructural parameters and the mechanical behavior of polar firm,
578 and when the onset of recrystallization occurs during creep, as well as verify the SRMin predicted
579 by the relationship of SRMin vs. temperature from the firm specimens at more extensive ranges of
580 stresses and temperatures.



581 **Appendix A:** Hydrostatic pressure, the applied stress, and the effective stress

582 The hydrostatic pressure, p , was calculated from the overburden of snow, using $p = \bar{\rho}_f gh$, where
583 $\bar{\rho}_f$ is the average firm density above the depth of interest, h , and g is the acceleration of gravity.
584 At Summit, p at the depths of 20 m, 40 m, and 60 m was estimated to be ~ 0.1 MPa, ~ 0.22 MPa,
585 and ~ 0.38 MPa, respectively. Note that the slope of the surface of ice sheets and glaciers at
586 Summit is idealized to be zero, i.e. their surfaces are horizontal. The applied stress, σ , is the
587 applied load divided by the cross-sectional area of a sample. The σ at the depths of 20 m, 40 m,
588 and 60 m were 0.21 MPa, 0.32 MPa, and 0.43 MPa, respectively. The effective stress, $\bar{\sigma}$, is
589 defined as σ divided by the fraction of ice matrix in firm, see in detail from Li and Baker
590 (2022a). Thereby, $\bar{\sigma}$ is 0.32 MPa (the mean porosity of 34.9%), 0.43 MPa (24.8%), and 0.5
591 MPa (14.4%) from the 20–60 m samples, respectively. Note that the stresses were vertically
592 loaded on the sample (parallel to the direction of core axis of the sample) in laboratory tests.
593 Ideally, in order to be analogous to the densification of firm in nature, $\bar{\sigma}$ for laboratory samples
594 from a given depth should be equal to the p of firm *in situ* at an equivalently same depth at
595 Summit, namely $\bar{\sigma}/p = 1$. However, in consideration of the laboratory timeframe for experiments
596 (Pimienta and Duval, 1987), the stresses applied in laboratory tests are usually higher with a
597 resulting higher rate of deformation than those *in situ*. Thus, to observe the effect of the stress on
598 the creep of firm with different densities at different depths, we designed the following
599 configuration of the $\bar{\sigma}/p$ with depth, viz., $0.32 \text{ MPa}/\sim 0.1 \text{ MPa} = \sim 3.2$, $0.43 \text{ MPa}/\sim 0.22 \text{ MPa} =$
600 ~ 1.95 , and $0.5 \text{ MPa}/\sim 0.38 \text{ MPa} = \sim 1.32$ for the samples from the depths of 20 m, 40 m, and 60 m,
601 respectively. In this manner, the decrement of $\bar{\sigma}/p$ with increasing depth represents the decrease
602 of the effective stress with increasing depth.



603 **Appendix B:** Strain rate minimum inferred via two kinds of constraints

604 To improve the reliability of inferred SRMins, two kinds of constraints were applied. First, the
605 SRMins from the -5°C and -18°C samples are calibrated using Glen' law $\dot{\epsilon}=A\sigma^n$ with $n = 4.3$
606 (Li and Baker, 2022a). PC1-SRMin, PC2-SRMin, and PC3-SRMin indicate three possibilities of
607 the SRMins that are calculated in turn from the 20 m, 40 m, and 60 m samples via the *only*
608 SRMin observed at a given temperature (Table 2). As an example, for the -5°C samples there
609 exist three possibilities from three depths. 1) The SRMin observed from the 20 m sample in the
610 orange font with grey background is used to respectively calculate two other SRMins for the 40 m
611 and 60 m samples in the dark red font in the column of PC1-SRMin. 2) In the same manner as in
612 scenario 1), the SRMin observed from the 40 m sample is calculated in the column of
613 PC2-SRMin, and the SRMin observed from the 60 m sample is calculated in the column of
614 PC3-SRMin. 3) In the same manner as in scenarios 1) and 2), the SRMin is calculated for the –
615 18°C samples in the blue font with grey background in turn from three depths. Second, the SRMin
616 of the -30°C samples is inferred on the basis of the range of Q_c , i.e. from 44.8 kJ mol^{-1} (upper
617 bound) to 113 kJ mol^{-1} (lower bound), using the Arrhenius relation.



618 **Data availability**

619 The data supporting the conclusions in this study are available at <https://arcticdata.io/catalog>.

620

621 **Author contribution**

622 YL and IB designed the experiments and YL carried them out. YL analyzed the data and

623 visualized the relevant results. YL prepared the manuscript with contributions from all co-authors.

624

625 **Competing interests**

626 At least one of the (co-)authors is a member of the editorial board of The Cryosphere.

627

628 **Acknowledgements**

629 This work was sponsored by the National Science Foundation Arctic Natural Science grant

630 1743106. Y. L. is grateful to Ciao Fu for the great support and help in COVID-19. The authors

631 wish to thank Chris Polashenski, Zoe Courville and Lauren B. Farnsworth at USA-CRREL for

632 their help with storage of the firm cores. The authors acknowledge the use of the Ice Research

633 Laboratory (Director-Erland Schulson) at Dartmouth College.



634 **References:**

- 635 Adolph, A.C.C., Albert, M.R., 2014. Gas diffusivity and permeability through the firn column at
636 Summit, Greenland: measurements and comparison to microstructural properties. *T.*
637 *Cryosph.*, 8, 319–328, doi:10.5194/tc-8-319- 2014.
- 638 Albert, M.R., Shultz, E.F. and Perron, F.E., 2000. Snow and firn permeability at Siple Dome,
639 Antarctica. *Ann. Glaciol.* 31, 353-356.
- 640 Anderson, D.L., Benson, C.S., 1963. The densification and diagenesis of snow. In: Kingery, W.D.
641 (Ed.), *Ice and Snow*. Press, Cambridge, Massachusetts, M.I.T, pp. 391–411.
- 642 Arnaud, L., Gay, M., Barnola, J.M., Duval P., 1998. Imaging of firn and bubbly ice in coaxial
643 reflected light: a new technique for the characterization of these porous media. *J. Glaciol.*,
644 44(147), 326-332.
- 645 Baker, R.W., Gerberich, W.W., 1979. The effect of crystal size and dispersed-solid inclusions on
646 the activation energy for creep of ice. *J. Glaciol.*, 24(90), 179-194.
- 647 Barnes, P., Tabor, D., Walker, J.C.F., 1971. The friction and creep of polycrystalline ice. *Proc. Roy.*
648 *Soc. Lond. A* (324),127-155.
- 649 Bartelt, P., Von Moos, M., 2000. Triaxial tests to determine a microstructure-based snow viscosity
650 law. *Ann. Glaciol.*, 31, 457-462.
- 651 Brown, D.E., George, S.M., 1996. Surface and bulk diffusion of $H_2^{18}O$ on single-crystal $H_2^{16}O$ ice
652 multilayers. *J. Phys. Chem.* 100 (38) 15460–15469.
- 653 Burr, A., Ballot, C., Lhuissier, P., Martingrie, P., Martin, C.L., Philip, A., 2018. Pore morphology
654 of polar firn around closure revealed by X-ray tomography, *T. Cryosph.*, Copernicus, 12(7),
655 2481-2500. 10.5194/tc-12-2481-2018. hal-01864373.
- 656 Coleou, C., Lesaffre, B., Brzoska, J.B., Ludwig, W., Boller, E., 2001. Three-dimensional snow



- 657 images by X-ray microtomography, *Ann. Glaciol.*, 32, 75-81.
- 658 Courville, Z., Horhold, M., Hopkins, M. and Albert, M., 2010. Lattice-Boltzmann modeling of the
659 air permeability of polar firn. *J. Geophys. Res., Earth Surface*, 115(F4).
- 660 Gow, A.J., 1969. On the rates of growth of grains and crystals in South Polar firn. *J. Glaciol.*, 8(53)
661 241-252.
- 662 Cuffey, K.M., Paterson, W.S.B., 2010. *The Physics of Glaciers*, 4th edited. Elsevier Inc.
- 663 Duval, P. Ashby, M.F., Anderman, I., 1983. Rate-controlling processes in the creep of
664 polycrystalline ice. *The Journal of Physical Chemistry*, 87, 4066-4074.
- 665 Ebinuma, T., Maeno, N., 1987. Particle rearrangement and dislocation creep in a snow
666 densification process. *J Phys.(Paris)*, 48,Colloq. C1, 263–269.
- 667 Flin, F., Brzoska, J.B., Lesaffer, B., Coleou, C., Pieritz, R.A., 2004. Three-dimensional geometric
668 measurements of snow microstructural evolution under isothermal conditions. *Ann. Glaciol.*,
669 38, 39-44.
- 670 Freitag, J., Dobrindt, U., Kipfstuhl, J., 2002. A new method for predicting transport properties of
671 polar firn with respect to gases on the pore-space scale, *Ann. Glaciol.*, 35, 538-544.
- 672 Fujita, S., Hirabayashi, M., Goto-Azuma, K., Dallmayr, R., Satow, K., Zheng, J., Dahl-Jensen, D.,
673 2014. Densification of layered firn of the ice sheet at NEEM, *J. Glaciol.*, 60 (223), 905-921,
674 doi:10.3189/2014JoG14J006.
- 675 Glen, J.W., 1955. The creep of polycrystalline ice, *Proceedings of the Royal Society A*, 228(1175),
676 519-538, doi.10.1098/rspa.1955.0066.
- 677 Goldsby, D.L., Kohlstedt, D.L., 2001. Superplastic deformation of ice: experimental observations,
678 *J. Geophys. Res.*, 106(B6), 11017-11030.
- 679 Goodman, D.J., Frost, H.J., Ashby, M.F., 1981. The plasticity of polycrystalline ice, *Philos. Mag.*,



- 680 A43 665–695.
- 681 Hildebrand, T., Ruegsegger, P. 1997. A new method for the model-independent assessment
682 of thickness in three-dimensional images. *J. Microsc.*, 185, 67-75.
- 683 Hobbs, P.V., 1974. *Ice Physics*, 1st edited. Oxford University Press Inc., New York.
- 684 Homer, D.R., Glen, J.W., 1978. The creep activation energies of ice. *J. Glaciol.*, 21(85), 429-444.
- 685 Hooke, R.L., Mellor, M., Budd, W.F., Glen, J.W., Higashi, A., Jacka, T.H., Jones, S.J., Lile, R.C.,
686 Martin, R.T., Meier, M.F., Russell-Head, D.S., Weertman, J., 1980. Mechanical properties of
687 polycrystalline ice: an assessment of current knowledge and priorities for research. *Cold Reg.*
688 *Sci. Technol.*, 3, 263-275.
- 689 Jacka, T.H., Li, J., 2000. Flow rates and crystal orientation fabrics in compression of
690 polycrystalline ice at low temperatures and stresses, *Physics of Ice Core Records*
691 *International Symposium on Physics of Ice Core Records*. Shikotsukohan, Hokkaido, Japan,
692 83-102.
- 693 Jumawan, A.B., 1972. An experimental study of self-diffusion in polycrystalline ice. *Diss.Abstr.*
694 *Int. B* 32, 5163–5164 (Abstract).
- 695 Landauer, J.K., 1958. The creep of snow under combined stress, *Transactions of the society of*
696 *rheology* II 175-194.
- 697 Li, J., Jacka, T.H., Budd, W.F., 1996. Deformation rates in combined compression and shear for
698 ice which is initially isotropic and after the development of strong anisotropy. *Ann. Glaciol.*,
699 23, 247-252.
- 700 Li, Y., Baker, I. 2021. Dynamic observations of the densification of polar firn under compression
701 using a micro-computed tomograph, *J. Geophys. Res., Earth Surface*, 126, e2021JF006290.
702 [doi:org/10.1029/2021JF006290](https://doi.org/10.1029/2021JF006290).



- 703 Li, Y. 2022. Critical values of the microstructural parameters at the first critical density of the
704 densification of polar firn. *Cold Reg. Sci. Technol.*, 198(2022), 10355.
705 doi.org/10.1016/j.coldregions.2022.103553.
- 706 Li, Y., Baker, I. 2022a. Observations of the creep of polar firn. *J. Glaciol.*, 68(268), 269–287.
707 doi.org/10.1017/jog.2021.91.
- 708 Li, Y., Baker, I. 2022b. Metamorphism observation and model of snow from Summit, Greenland
709 under both positive and negative temperature gradients in a Micro CT, *Hydrol. Processes*,
710 e14696. doi.10.1002/HYP.14696.
- 711 Li, Y. 2023a. Are bubbles in ice the potential space for hydrogen storage? *Int. J. Hydrogen*
712 *Energy*, 50(D), 575-585. doi.org/10.1016/j.ijhydene.2023.07.273.
- 713 Li, Y. 2023b. Changes in grain size during the relaxation stage of viscoelastic firn, *Philos. Mag.*,
714 104(4), 239-259. doi.org/10.1080/14786435.2023.2296656.
- 715 Li, Y., Fu, C., Keegan, C. et al. 2023. Microstructural characterization of depth hoar and ice-crust
716 layers using a micro-CT, and hypothesis of ice-crust formation under a thunderstorm, *Hydrol.*
717 *Processes*, 37(12), e15060. doi.org/10.1002/hyp.15060.
- 718 Li, Y. 2024. The improvement of hydrogen storage capacity via bubbles nucleated in ice-like
719 nanotubes, *Mater. Today Sustainability*, 27, 100856.
- 720 Li, Y., Fu, C. 2024. Determination of the critical grain size from the deformation of polar firn.
721 *Am. Mineral.* (In review).
- 722 Liu, K., Sun, R. & Daraio, C. 2022. Growth rules for irregular architected materials with
723 programmable properties. *Sci.*, 377(6609), 975-981.
- 724 Mellor, M., Smith, J.H., 1966. Creep of snow and ice, *CRREL Res. Rep.* 220.
725 Mellor, M., Testa, R., 1969. Effect of temperature on the creep of ice. *J. Glaciol.*, 8(52), 131-145.
- 726 Nasello, O.B., Di Prinzio, C.L., Guzman, P.G., 2005. Temperature dependence of “pure” ice grain



- 727 boundary mobility, *Acta Mater.*, 53(18) 4863–4869, doi: 10.1016/j.actamat.2005.06.022.
- 728 Ogunmolasuyi, A., Murdza, A., Baker, I. 2023. The onset of recrystallization in polar firn.
729 *Geophys. Res. Lett.*, 50, e2023GL103435. doi.org/10.1029/2023GL103435.
- 730 Paterson, W.S.B., 1977. Secondary and tertiary creep of glacier ice as measured by borehole
731 closure rates, *Rev. Geophys. Space Phys.*, 15, 47–55.
- 732 Perutz, M.F., Seligman, G., 1939. A crystallographic investigation of glacier structure and the
733 mechanism of glacier flow. *Proc. Roy. Soc. London A* 172, 335–360.
- 734 Pimienta, P., Duval, P., 1987. Rate controlling processes in the creep of polar glacier ice. *Journal*
735 *de Physique*, 48, 243-248.
- 736 Salamatin, A.N., Lipenkov, V.Y., Barnola, J.M., Hori, A., Duval, P., Hondoh, T. 2009. Snow/firn
737 densification in polar ice sheets. In: Hondoh, T. (Ed.), III. Firn densification, close-off and
738 chronology, 195-222, Hokkaido University Press.
- 739 Scapozza, C., Bartelt, P.A., 2003. The influence of temperature on the small-strain viscous
740 deformation mechanics of snow: a comparison with polycrystalline ice. *Ann. Glaciol.*, 37,
741 90–96.
- 742 Schleeß, S., Lowe, H., Schneebeli, M., 2014. Influence of stress, temperature and crystal
743 morphology on isothermal densification and specific surface area decrease of new snow. *T.*
744 *Cryosphy.*, 8, 1825-1838.
- 745 Sinha, N.K., 1978. Short-term rheology of polycrystalline ice. *J. Glaciol.*, 21(85) 457-472.
- 746 Vickers, W., Greenfield, P., 1968. The high temperature creep properties of compacted
747 magnesium powder. *Journal of Nuclear Materials*, 27(1), 73-79.
- 748 Wang, X., Baker, I., 2013. Observation of the Microstructural Evolution of Snow under Uniaxial
749 Compression using X-ray Computed Micro-tomography, *J. Geophys. Res.*, 118, 1-12,
750 doi.org/10.1002/2013JD020352.



- 751 Weertman, J., 1983. Creep deformation of ice. *Annual Review Earth Planet Science*, 11, 215–240.
- 752 Wiese, M., Schneebeli, M., 2017. Snowbreeder 5: a Micro-CT device for measuring the
753 snow-microstructure evolution under the simultaneous influence of a temperature gradient
754 and compaction. *J. Glaciol.*, 63(238), 355–360, doi: 10.1017/jog.2016.143.